Applied Catalysis B: Environment and Energy 368 (2025) 125140

Contents lists available at ScienceDirect

Applied Catalysis B: Environment and Energy

journal homepage: www.elsevier.com/locate/apcatb

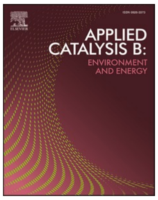

Medium-entropy alloy design enables highly efficient catalytic methanolysis of ammonia borane

Fei Chu [b,c,1], Jiahuan He [e,1], Jinze Wang [b,c], Nuo Lei [b,c], Sicheng Yuan [b,c], Shuoqing Zhang [b,c], Lixin Chen [b,c,d], Xuezhang Xiao [a,b,c,d,*]

[a] School of Advanced Energy, Sun Yat-Sen University, Shenzhen 518107, China
[b] School of Materials Science and Engineering, Zhejiang University, Hangzhou 310058, China
[c] State Key Laboratory of Silicon and Advanced Semiconductor Materials, Zhejiang University, Hangzhou 310058, China
[d] Key Laboratory of Hydrogen Storage and Transportation Technology of Zhejiang Province, Hangzhou 310027, China
[e] Institute of Materials, China Academy of Engineering Physics, Mianyang, Sichuan 621908, China

ARTICLE INFO

Keywords:
Ammonia borane
Methanolysis
Medium-entropy alloys
Catalyst

ABSTRACT

In this study, a non-noble metal based CuCoNi medium-entropy alloy (MEA) catalyst is innovatively applied for hydrogen production via ammonia borane (AB) methanolysis. The optimized component of the CuCoNi MEA is determined through theoretical calculation by tuning the *d*-band center of alloys, and the catalysts are synthesized using rapid carbothermal shock (CTS) method, enabling the formation of MEA nanoparticles with small size and uniform composition. The CuCoNi MEA catalyst exhibits superior catalytic activity in AB methanolysis, with an activation energy of 35.1 kJ mol^{-1} and a turnover frequency value (TOF) of 32.65 $mol_{H2}\ mol_{cat}^{-1}\ min^{-1}$ at 30 °C, outperforming the relevant binary and unary counterparts. The exceptional catalytic activity and stability are attributed to the multi-component alloy structure and increased mixing entropy of Cu/Co/Ni. This study provides guidance for designing high-performance catalysts for AB methanolysis and promotes the integrated device application of AB in rapid hydrogen production at room temperature.

1. Introduction

Hydrogen energy is regarded as a promising substitute for fossil energy to solve the energy crisis. An important application of hydrogen is in hydrogen fuel cells, which can be used for powering vehicles [1–5]. Ammonia borane (NH_3BH_3, hereafter abbreviated as AB) has the potential to serve as a safe hydrogen storage material due to its high hydrogen content (19.6 wt%), solid-state form, and stability at room temperature [6,7]. Hydrogen generation from AB can be achieved via pyrolysis, hydrolysis, and methanolysis. Among these methods, pyrolysis requires high temperatures, whereas both hydrolysis and methanolysis can proceed at room temperature using catalysts [8–10]. Compared to hydrolysis, AB methanolysis avoids the production of ammonia gas, which is detrimental to hydrogen fuel cells. Additionally, AB has higher solubility in methanol than in water. Moreover, the low freezing point of methanol (-97.8 °C) endows hydrogen generation via AB methanolysis with application potential in extremely cold areas [11–14]. Based on the above advantages, AB methanolysis is a promising technology for hydrogen production.

Abundant active and durable catalysts for hydrogen generation via AB methanolysis have been extensively studied and reported over the past few decades [15–18]. Although the low cost of non-noble metal catalysts endows the potential for large-scale application compared to noble metal catalysts, their catalytic performance is often hindered by the intrinsic poor atomic activity. To overcome this limitation, multiple components have become an important approach to enhance the performance of non-noble metal catalysts. Nanoscale high-entropy alloys (HEAs) and medium-entropy alloys (MEAs) have shown great potential in the field of catalysis, including water splitting [19–22], CO_2 reduction [23], and dye degradation [24], etc., due to their extraordinary catalytic activity and stability promoted by the unique “high entropy effects” and “cocktail effects” [25–29]. HEAs provide numerous active sites for catalytic reactions, enabled by their multi-element composition and random atomic arrangement. Additionally, the varying atomic sizes in HEAs lead to lattice distortion, further generating more active sites [30, 31]. The carbothermal shock (CTS) synthesis method reported by Hu

---

* Corresponding author at: School of Advanced Energy, Sun Yat-Sen University, Shenzhen 518107, China.
E-mail address: xiaoxzh6@mail.sysu.edu.cn (X. Xiao).

[1] Fei Chu and Jiahuan He contributed equally.

https://doi.org/10.1016/j.apcatb.2025.125140
Received 9 December 2024; Received in revised form 5 February 2025; Accepted 6 February 2025

and coworkers has greatly promoted the development of nanoscale HEAs in catalysis [32]. Therefore, enhancing the catalytic activity of non-noble metal catalysts through the multi-component strategy offers a promising approach for designing high-activity and low-cost catalysts, enabling the potential of large-scale hydrogen production via AB methanolysis.

Herein, we selected the transition metals Cu, Co, and Ni as the active component to synthesize alloy catalysts for AB methanolysis, owing to their low cost and considerable catalytic activities [33–35]. Furthermore, their similar atomic radii and lower heat of formation facilitate the formation of stable MEA structures [36]. The electronic properties of Cu/Co/Ni alloys were investigated using the first-principles calculation based on density functional theory (DFT). By adjusting the *d*-band center of the catalyst to be located between the HOMO site of AB and the LUMO site of methanol, rapid electron transfer between AB and methanol can be achieved, resulting in high catalytic dehydrogenation efficiency. DFT simulation results indicate that the CuCoNi equimolar alloy component can exhibit the highest catalytic activity compared with their pure metal and binary alloy counterparts in AB methanolysis. Based on these guidelines, we further prepared CuCoNi medium-entropy alloy nanoparticles (MEA NPs) supported on CO_2-activated carbon nanospheres (CAC) with an average diameter of 15.8 nm using the CTS method and introduced them into the AB methanolysis process. It is demonstrated that the CuCoNi MEA NPs@CAC catalyst possesses excellent catalytic ability in hydrogen generation with a TOF value of 32.65 $mol_{H2}\ mol_{cat}^{-1}\ min^{-1}$ at 30 °C and an activation energy of 35.1 $kJ\ mol^{-1}$. The TOF value of CuCoNi MEA NPs@CAC is 1.6, 1.4, and 2.5 times that of CuNi NPs@CAC, CoNi NPs@CAC and Ni NPs@CAC samples respectively. Furthermore, the cyclic catalytic stability of the CuCoNi MEA NPs@CAC is significantly improved compared to the Ni NPs@CAC catalyst. In this work, we introduce MEA NPs as an advanced catalyst in AB methanolysis for the first time, significantly enhancing hydrogen energy applications, particularly in fuel cell vehicles.

2. Experimental section

2.1. Materials

All the chloride precursors, copper (II) chloride dihydrate ($CuCl_2 \cdot 2\ H_2O$, 99.99 %), cobalt (II) chloride hexahydrate ($CoCl_2 \cdot 6\ H_2O$, 99.9 %), nickel (II) chloride hexahydrate ($NiCl_2 \cdot 6\ H_2O$, 99.99 %), AB (NH_3BH_3, >97 %) were purchased from Aladdin Chemical Co. Ltd without further purification. Carbon nanospheres (BP-2000, Cabot Corporation), carbon cloth (W0S1009, CE-Tech Co. Ltd.), sodium borohydride ($NaBH_4$, >96 %, Sinopharm Co. Ltd.), ethanol absolute (C_2H_6O, GR, Sinopharm Co. Ltd.), Methanol (CH_4O, AR, Sinopharm Co. Ltd.), Methanol-D (CH_3OD, >99 atom % D, Sigma-Aldrich Co. Ltd.) were used as received.

2.2. Carbon support preparation

The CAC supports were prepared according to a previously reported procedure [37]. The carbon nanospheres were placed in a tubular furnace and heated to 800 °C at a ramp rate of 10 °C min^{-1} and then held for 1 h in a CO_2 flow. After cooling to room temperature, the black powder was collected to obtain CO_2-activated carbon nanospheres, which are denoted as CAC.

2.3. Catalyst preparation

The CuCoNi MEA NPs@CAC samples were synthesized by the CTS method, where high temperatures generated from an electric pulse generator were used to shock the mixed metal precursors to form MEAs and generated on the carbon supports. The metal precursor solution was obtained by mixing $CuCl_2 \cdot 2\ H_2O$, $CoCl_2 \cdot 6\ H_2O$, and $NiCl_2 \cdot 6\ H_2O$ (0.025 M, respectively) in a molar ratio of 1:1:1, and then absolute ethanol was added, followed by magnetic stirring to dissolve. After metal chlorides were completely dissolved, each metal ions solution with the same volumes (0.67 mL, 2 mL, and 6 mL) was added to 72 mg of CAC and mixed well to obtain the metal precursors mixture with different total metal amounts (0.05, 0.15, and 0.45 mmol). Coating the mixture evenly on a rectangular carbon cloth of 4 * 6 cm size, then dried and divided into 12 equal parts. Take one piece of 1 * 2 cm carbon cloth and connect it to the self-made controllable circuit. A DC power supply and an electric pulse generator (capacitor) were connected to the circuit. The charging current was kept at 3.6 A, and the charge voltage was adjusted to change the electrical pulse. In an argon atmosphere, the electric pulse generator quickly discharged to achieve high-temperature thermal shock on carbon cloth, and the metal precursor decomposed to form MEAs. The powder on the carbon cloth was scraped off to obtain the supported MEA NPs catalyst $CuCoNi_{(n)}$ MEA NPs@CAC (*n* is the total mole amounts of added CuCoNi metal with the unit of mmol). The binary CuCo/CuNi/CoNi alloy and the unary Cu/Co/Ni alloy NPs@CAC catalysts were prepared similarly, except that the precursor solution was replaced with the corresponding components. To ensure an accurate and scientific comparison, the total molar amount of metal precursor in preparing unary and binary alloy NPs was the same as that of CuCoNi MEA NPs.

The CuCoNi MEA NPs@CAC were also prepared by a traditional wet chemical reduction method for comparison. Specifically, 72 mg of CAC were ultrasonically dispersed in 10 mL absolute ethanol for 30 min. Then, each metal precursor solution of Cu/Co/Ni was added to the above suspension with a volume of 2 mL. After magnetic stirring for 4 hours, a fresh $NaBH_4$ solution (0.6 M, 2.5 mL) was added with stirring for a further 1 hour to reduce the metal precursor to deposited on the CAC supports. The product was washed and collected by centrifugation and then dried at 50 °C overnight to obtain CuCoNi MEA NPs@CAC-reduction.

2.4. Catalyst characterization

The microscopic morphology of the samples was observed by scanning electron microscope (SEM, Hitachi SU-70 microscopy). The microstructure and element distribution of the prepared samples were investigated by the transmission electron microscope (TEM, FEI Tecnai F20 microscopy) and (JEOL JEM F200 JEOL, Japan) equipped with two JEOL energy dispersive X-ray spectrometers (super-EDS) at 200 kV. Powder X-ray diffraction (XRD, PANalytical/X'Pert pro, Cu K_α radiation, 40 kV, 150 mA) was used to analyze the phase and structure of materials. X-ray photoelectron spectroscopy (XPS) was performed on a Thermo Scientific ESCALAB 250Xi with Al K_α radiation to get the chemical state of the sample. The N_2 adsorption-desorption isotherms were performed on a Quantachrome NOVA 1000e instrument to determine Brunauer-Emmett-Teller (BET) specific surface area. An infrared thermometer (Optris CT-3MH3) was used to detect temperature changes in the CTS method. Inductively coupled plasma atomic emission spectroscopy (ICP-OES, Thermo-iCAP6300) was employed to analyze the actual metal content in the catalyst.

2.5. Catalytic experiments

25 mg of prepared catalyst and 4 mL of methanol were placed in a 50 mL double-necked round bottom flask. One neck of the flask was equipped with a sealing rubber stopper, allowing the addition of AB solution into the reactor via a microinjector. The other neck was connected to a 1000 mL sealed glass bottle filled with water through a condensing tube. The generated hydrogen would drain an equal volume of water and flow into a glass bottle placed on an electronic balance. The balance can continuously monitor the mass change in real time and record it on the computer. Catalytic reaction was carried out in a bath at 30 °C with a rotation rate of 600 r min^{-1}. 30 mg of AB was dissolved in 0.5 mL of methanol and injected into the catalyst solution, which was

recorded as the start of the reaction. The volume of hydrogen generation was calculated based on the mass of the drained water, and the catalytic activity was evaluated by comparing the time required to release the same amount of hydrogen. The TOF values in the hydrogen generation reaction via AB methanolysis are calculated by the following equation:

$$\mathrm{TOF} = \frac{n(\mathrm{H_2})}{n(\mathrm{Cu+Co+Ni})\cdot t} \tag{1}$$

Here, $n(\mathrm{H_2})$ represents the mole of hydrogen generation during 0–2 mmol, and $n(\mathrm{Cu+Co+Ni})$ is the total actual metal amount of the catalyst according to ICP-OES results for the AB methanolysis reaction. t represents the time required to produce 2 mmol of hydrogen.

To test the durability of the catalyst, a fresh AB solution was injected after the initial reaction and this procedure would continuously repeat. Furthermore, the activation energy of the AB methanolysis catalytic reaction was determined by reactions carried out at different temperatures (20 °C, 25 °C, 30 °C, and 35 °C).

2.6. Theoretical computations

The periodic density functional theory (DFT) calculations were employed using the Vienna ab initio simulation package (VASP) with the projector-augmented wave (PAW) method [38,39]. The generalized gradient approximation (GGA) with Perdew, Burke, and Ernzerhof (PBE) realization was used for the exchange-correlation function. The energy cutoff was set above 350 eV, and the force and energy convergence criteria were set to 0.02 eV/Å and 10^{-5} eV respectively. The long-range dispersion was accounted for using the DFT-D3 corrections. The (111) facets of Ni, CuNi, CoNi, and CuCoNi were cleaved, slab models were created and optimized, and a vacuum of 15 Å was used for each slab to avoid interaction between neighboring slab images. The DOS of Ni, CuNi, CoNi, CuCoNi, AB, and CH_3OH were calculated and corrected with the energy of the vacuum level. The climbing image nudged elastic band (CI-NEB) method was employed to study the energy barrier of CH_3OH decomposition. In order to compare the electronic structures of different systems, the density of states for different systems relative to the vacuum energy level ($E_{\mathrm{DOS\text{-}VAC}}$) were calculated according to the following formulas [40]:

$$\Phi = E_{\mathrm{VAC}} - E_{\mathrm{F}} \tag{2}$$

$$E_{\mathrm{DOS\text{-}VAC}} = E_{\mathrm{DOS\text{-}F}} - \Phi \tag{3}$$

Where Φ is the electron work function, E_{VAC} is the vacuum energy level, E_{F} is the Fermi energy level, $E_{\mathrm{DOS\text{-}VAC}}$ is the density of state relative to the vacuum energy level and $E_{\mathrm{DOS\text{-}F}}$ is the density of state relative to the Fermi energy level.

3. Results and discussion

3.1. Composition design by theoretical calculation

Hydrogen evolution from AB methanolysis involves the combination of H^+ from the O-H in methanol and H^- from the B-H in AB. The O-H3 and B-H2 bonds are activated and subsequently broken by the catalyst

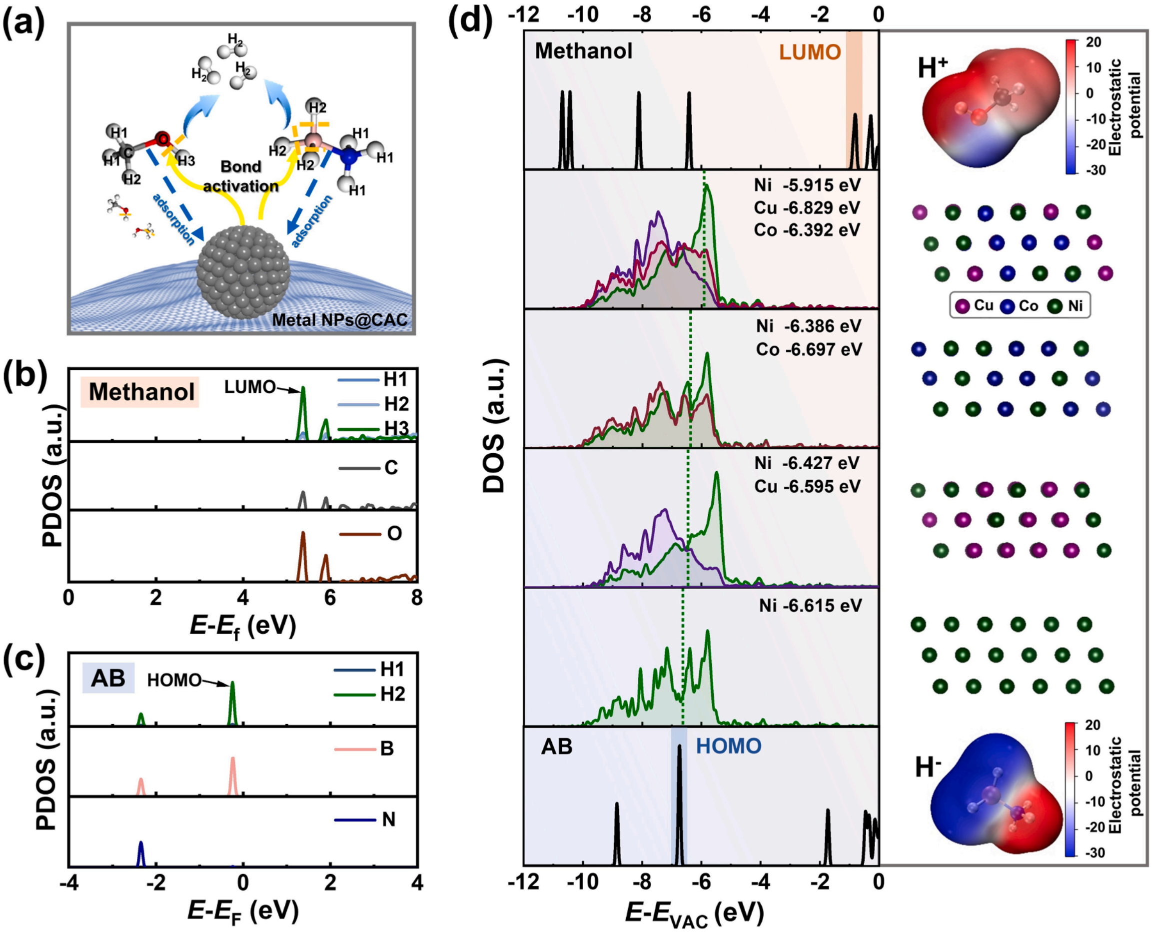

Fig. 1. a) Mechanism for metal NPs@CAC catalyzing AB methanolysis. The *d*-orbital PDOS spectrum of the b) methanol and c) AB molecular. d) Up and down: The DOS of the methanol and AB molecules, along with their electrostatic potential distribution diagrams. Middle: The DOS of the CuCoNi, CoNi, CuNi, and Ni alloys respectively, along with the structure models of these alloys.

during the AB methanolysis reaction, as shown in molecular models in Fig. 1a [15,41,42]. Electron transfer between AB and methanol is facilitated by the catalyst, promoting dehydrogenation and the formation of H_2. Specifically, the projected density of states (PDOS) of AB and methanol indicate that the O and H3 atoms of methanol primarily contribute to the LUMO site (Fig. 1b), while the B and H2 atoms of AB mainly contribute to the HOMO site (Fig. 1c). Therefore, the HOMO site of AB and the LUMO site of methanol are considered the catalytically active orbitals that determine the catalytic activity of AB and methanol. When the *d*-orbital of the catalyst is positioned between the HOMO of AB and the LUMO of methanol, it can significantly enhance electron transfer efficiency, thereby improving catalytic activity [43]. Cu/Co/Ni non-noble metal catalysts are commonly used in AB hydrogen evolution systems. To study the optimal catalytic structure of Cu/Co/Ni active components, we construct the Ni, CuNi, CoNi, and CuCoNi models for DOS calculations, as shown in Fig. 1d. The electrostatic potential distribution diagrams of methanol and AB reveal that the O-H3 and B-H2 atoms exhibit opposite charges, confirming that charge transfer between the two reactants would facilitate the H^+ and H^-, leading to the formation of H_2. The DOS of Cu, Co, and Ni atoms is compared to the molecular orbital energy levels of AB and methanol. The *d*-band center of the Ni unary alloy is closer to the HOMO of AB but is far from the LUMO of methanol. However, with the addition of Cu or Co atoms, the *d*-band center of Ni shifts to a higher energy level, bringing it closer to the LUMO site of methanol. Moreover, when both Cu and Co are added, the *d*-band center of Ni shifts to the position closest to the LUMO site, compared to the Ni unary alloy and CuNi/CoNi binary alloys. This result indicates that Ni in the CuCoNi MEA significantly facilitates electron transfer between the HOMO site of AB and the LUMO site of methanol. Therefore, the CuCoNi MEA alloy is expected to exhibit the highest catalytic activity for AB methanolysis among the Ni-based non-noble metal catalysts discussed. Notably, the order of the three alloy components in the CuCoNi MEAs, based on their proximity to the LUMO site, is Ni, Co, and Cu. Hence, it is proposed that the catalytic activity of the monometallic components follows the order: Ni > Co > Cu.

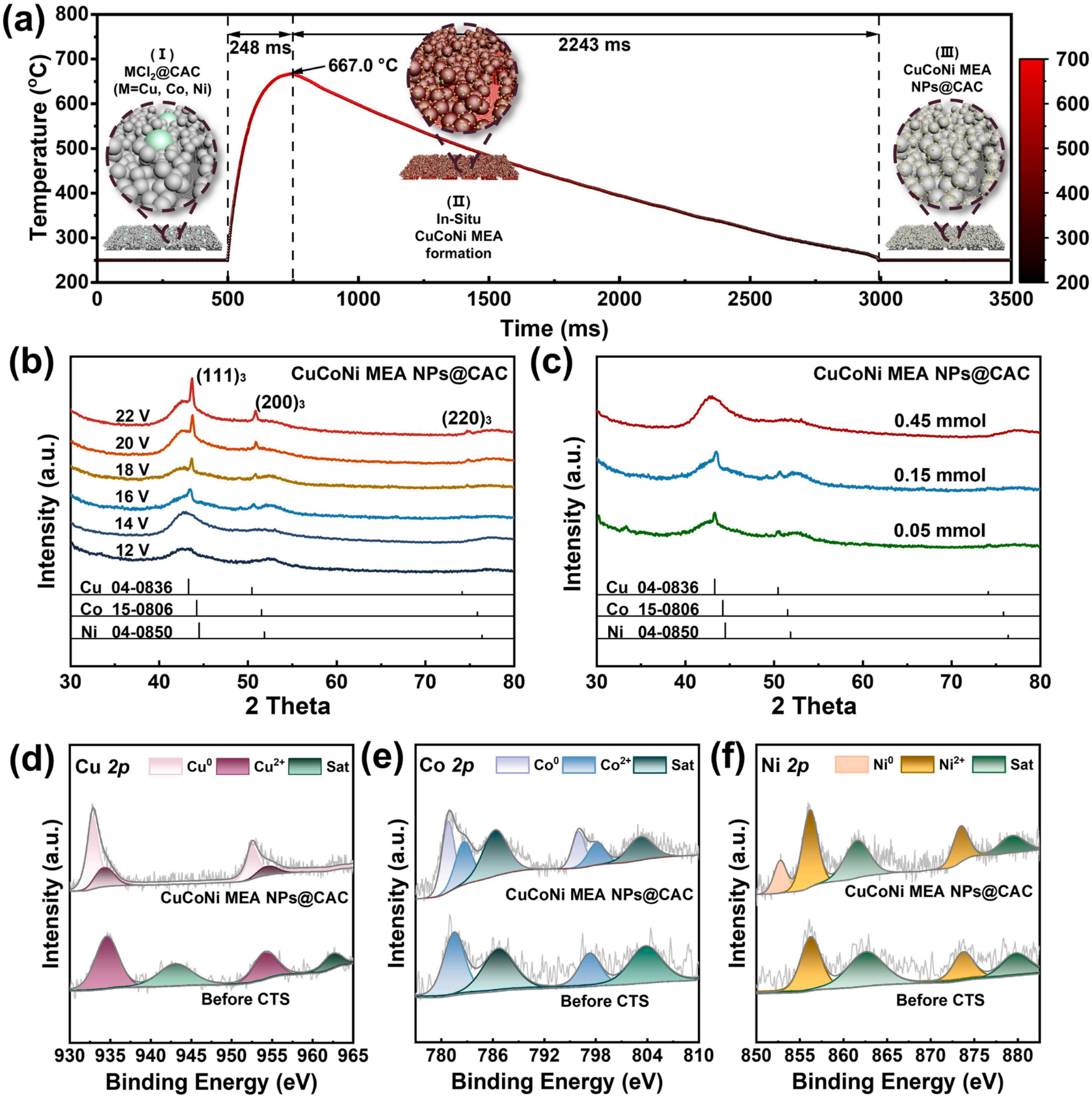

Fig. 2. a) Temperature-time curve of the CTS process with the voltage of 16 V, inserted the schematic illustration of the CuCoNi MEA NPs@CAC generation procedure. b) XRD patterns of the $CuCoNi_{(0.15)}$ MEA NPs@CAC prepared at different discharge voltages. c) CuCoNi MEA NPs@CAC prepared with different metal loadings at 16 V. d-f) XPS spectra of Cu 2*p*, Co 2*p*, and Ni 2*p* of $CuCoNi_{(0.15)}$ MEA NPs@CAC before and after16 V CTS treatment.

3.2. Synthesis and characterization

To verify the DFT simulation results and further investigate the catalytic performances of CuCoNi MEA, a series of CuCoNi MEA NPs catalysts was prepared by the CTS method. The schematic diagram of CuCoNi MEA NPs@CAC synthesis is shown in Fig. S1. Initially, metal precursor solutions were homogeneously mixed with CAC and coated onto carbon cloth. With a rapid temperature rise and fall achieved by capacitor discharge (Fig. 2a), the metal precursor ions ($Cu^{2+}/Co^{2+}/Ni^{2+}$) transformed into MEAs and generated on CAC to form the CuCoNi MEA NPs@CAC. The synthesis temperature was measured by an infrared thermometer and the temperature-voltage relationship is depicted in Fig. S2. As shown in Fig. 2b, under the same metal loading, increasing the discharge voltage led to the generation and intensification of diffraction peaks at 44.2°, 51.6°, and 76.2°, corresponding to the (111), (200), and (220) planes of the FCC single-phase CuCoNi MEA [44, 45]. Notably, the broad diffraction peak around 43° is corresponding to the CAC support, which can be confirmed by the XRD comparison in Fig. S3. Fig. S4 shows the TEM images of CuCoNi NPs@CAC prepared at discharge voltages of 12 V, 16 V, and 20 V. At 12 V, only a few scattered particles were observed. As the voltage increases to 16 V, numerous round particles are generated evenly on the CAC support. Further increasing the voltage to 20 V led to significant particle growth. Considering that excessively high temperatures promote particle growth, which can be detrimental to catalytic activity, it is necessary to determine an optimal discharge voltage to yield well-formed MEA NPs of suitable size. The 16 V discharge voltage, where alloy diffraction peaks first appeared during the ramp-up experiment, was selected for further investigation.

The metal loading also affects the formation of MEA NPs. Fig. 2c shows the XRD patterns of CuCoNi MEA NPs prepared at 16 V with varying metal precursor additions. Distinct diffraction peaks appeared when the metal precursor amounts were 0.05 mmol and 0.15 mmol, confirming the formation of MEAs. However, when the loading was increased to 0.45 mmol, no significant diffraction peaks were observed, due to the insufficient heat generation at the same voltage to convert the excess metal ion precursors into MEAs. Based on the XRD results, a theoretical metal loading of 0.15 mmol was selected for subsequent study to balance a higher metal loading with the stable MEA formation. Figs. 2d-2f present the XPS spectra of the $CuCoNi_{(0.15)}$ MEA NPs@CAC before and after CTS treatment. All three metal elements before CTS completely show a divalent chemical state, corresponding to the

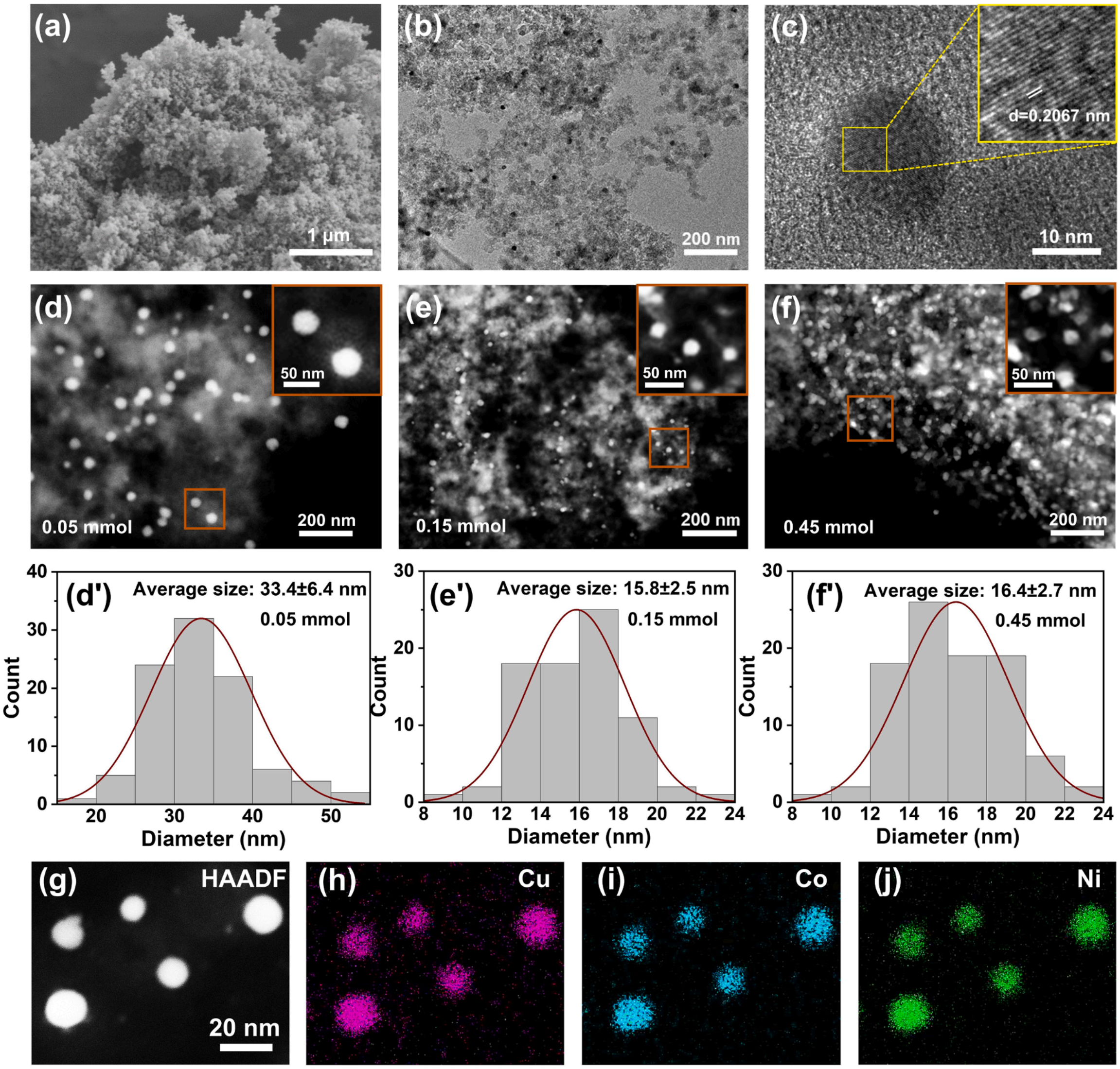

Fig. 3. a-b) SEM and TEM images of the CuCoNi MEA NPs@CAC. c) HR-TEM image of a CuCoNi MEA NP located in the CAC support, inserted the lattice spacing. d-f) HAADF-STEM images and size distribution plots of the CuCoNi MEA NPs@CAC prepared with different metal loadings at 16 V. g-j) HAADF-STEM image and EDS mappings of the $CuCoNi_{(0.15)}$ MEA NPs@CAC prepared at 16 V.

precursor metal ions [46,47]. After the CTS process, the appearance of zero-valence peaks for all three elements indicated the successful formation of CuCoNi MEAs. A little oxidation state in the XPS signal can be attributed to the charge flowing among the Cu, Co, and Ni atoms and the electronic interactions with CAC [48].

The overall micromorphology of the catalyst is coral-like as observed in Fig. 3a, which is mainly composed of stacked spherical CAC particles. Unlike the previous CTS method, in which the metal chlorides were directly loaded onto carbon cloth, CAC here serves as a three-dimensional catalyst support with excellent electrical conductivity and high specific surface area. As shown in Fig. S5, the CAC support has a specific surface area of 1309 $m^2 g^{-1}$ with a pore volume of 2.02 $cm^3 g^{-1}$. After loading, CuCoNi MEA NPs occupied the surface pores of CAC, reducing the specific surface area significantly to 884 $m^2 g^{-1}$. The TEM image (Fig. 3b) shows that many NPs were formed and attached to the CAC surface, which also confirms the decrease in specific surface area. The high-resolution TEM image in Fig. 3c reveals the interplanar spacing of the alloy particle is 0.2067 nm, which is located between the lattice spacings of FCC Cu (0.2088 nm), Co (0.2046 nm) and Ni (0.2034 nm) alloys. These TEM results confirmed the successful synthesis of FCC single-phase CuCoNi MEA. Figs. 3d-3f are the high-angle annular dark-field scanning transmission electron microscopy (HAADF-STEM) images of the MEA NPs@CAC prepared with different theoretical metal loading, along with the corresponding particle size distribution plots. The average particle size of $CuCoNi_{(0.05)}$ MEA NPs is 33.4 nm, while the $CuCoNi_{(0.15)}$ (15.8 nm) and $CuCoNi_{(0.45)}$ (16.4 nm) MEA NPs are much smaller. Notably, the dispersibility of $CuCoNi_{(0.15)}$ is significantly better than that of $CuCoNi_{(0.45)}$, and $CuCoNi_{(0.45)}$ exhibits more irregular particle shapes, as the inserted enlarged views depicted. This indicates that the metal loading substantially affects the micromorphology of MEA NPs. By controlling the discharge voltage at 16 V, a consistent energy input is provided to the metal precursors with different loadings. When the loading is 0.05 mmol, the precursors receive a higher average energy, resulting in the formation of larger NPs. As the loading increases to 0.15 mmol, particle size decreases significantly, maintaining good dispersibility on the CAC surface. In sharp contrast, for the $CuCoNi_{(0.45)}$ sample, the energy input becomes insufficient to fully convert the excessive metal precursors into a stable MEA alloy, which can also be confirmed by the XRD result in Fig. 2c. Furthermore, the overabundant metal precursor addition caused severe particle agglomeration, which is one of the factors that negatively affect the performance of the NPs catalysts.

Herein, an optimized strategy for obtaining CuCoNi MEA NPs with superior micromorphology through adjustments in the discharge voltage and metal loading can be summarized as follows: (1) For a given metal loading, a higher discharge voltage provides greater energy input, promoting sufficient alloying but also driving particle growth; (2) With a constant discharge voltage, a lower metal loading endows more energy is available for each metal particle, resulting in larger particle sizes. However, an excessive amount of metal precursors will result in the energy input being unable to completely convert all the metal precursors into MEAs, leading to poor dispersion of the generated NPs. In conclusion, the degree of alloying and average particle size of CuCoNi MEA NPs are determined by the combined effect of discharge voltage and metal loading.

Figs. 3g-3j present the EDS mappings of the $CuCoNi_{(0.15)}$ MEA NPs prepared at 16 V, illustrating that the Cu, Co, and Ni elements precisely matched with the particles in the STEM image without any compositional inhomogeneity. The EDS area scanning result (Fig. S6) indicates that the molar ratio of Cu, Co, and Ni is close to 1:1:1. To determine the actual metal loading and elemental ratios accurately, the CuCoNi MEA NPs@CAC sample was analyzed using ICP-OES, and the results were compared with the theoretical loading (Table S1). The actual metal loading was slightly lower than the theoretical value, due to the depletion of metal ions while coating the precursor mixture onto the carbon cloth. Nevertheless, the ICP-OES results indicated that the actual ratio of Cu, Co, and Ni elements is 1:1.09:1.09, closely matching the intended 1:1:1 ratio. Combined with the XRD and XPS patterns in Fig. 2, it can be concluded that a homogeneous FCC single-phase CuCoNi MEA NPs@CAC was successfully synthesized.

3.3. Catalytic performance and reaction kinetics

The catalytic activity in AB methanolysis of the CuCoNi MEA NPs prepared with different discharge voltages and metal loading was investigated. Fig. 4a shows the hydrogen generation curves of the $CuCoNi_{(0.15)}$ MEA NPs@CAC catalysts prepared at different voltages. The corresponding TOF values were calculated based on the actual metal loading and presented in Fig. 4c. Compared with the sample prepared at 12 V and 20 V, the $CuCoNi_{(0.15)}$-16 V sample exhibits the fastest hydrogen generation performance, with a TOF of 32.65 min^{-1}. Combining the TEM images of these three samples (Fig S3), it can be concluded that only the MEA NPs with uniform distribution, sufficient quantity, and appropriately small size can achieve optimal catalytic activity. Fig. 4b illustrates the hydrogen generation curves of the CuCoNi MEA NPs@CAC catalysts prepared with different metal loading. Although the $CuCoNi_{(0.45)}$ sample completed hydrogen release in a shorter time, this was due to its higher metal loading. Similarly, the slower hydrogen release rate of $CuCoNi_{(0.05)}$ can be attributed to its lower loading. By calculating their TOF values based on actual metal amounts (Table S2), the sample with 0.15 mmol loading exhibits the highest catalytic efficiency. Further analysis of the TOF values in Fig. 4c reveals that the two samples with the lowest catalytic efficiency are $CuCoNi_{(0.15)}$-20 V and $CuCoNi_{(0.05)}$-16 V, with the TOF values of 13.51 min^{-1} and 13.76 min^{-1}, respectively. Microstructure characterization indicates that both samples contain relatively large particles (Fig S4 and Fig. 3d). In comparison, $CuCoNi_{(0.15)}$-12 V and $CuCoNi_{(0.45)}$-16 V display slightly better catalytic efficiency, with the TOF values of 21.89 min^{-1} and 20.82 min^{-1}, despite exhibiting indistinct alloy peaks in their XRD results. This finding suggests that excessively large particle size has a more detrimental impact than incomplete alloying on hydrogen generation through AB methanolysis. Based on the above results, $CuCoNi_{(0.15)}$-16 V MEA NPs@CAC was selected for further studies, as it demonstrated the highest catalytic activity and a stable MEA structure.

The catalytic performance results predicted by DFT simulations were validated through the following experiments. Under identical discharge voltage and metal loading conditions, unary Cu, Co, and Ni alloys, as well as binary CuCo, CuNi, and CoNi alloys NPs, were synthesized using CTS methods. Figs. 4d-4e present the hydrogen generation curves for the above samples. Among them, the CuCoNi MEA NPs@CAC demonstrated the highest catalytic efficiency compared to its unary and binary counterparts, confirming that the multi-component strategy effectively enhanced catalytic performance by modulating the *d*-band center. The actual metal amounts were measured by ICP-OES (Table S3). As shown in Fig. 4 f, TOF values indicate that the catalytic activity order is Ni>Co>Cu, with the TOF value of Ni (13.07 min^{-1}) being significantly higher than that of Co (2.87 min^{-1}) and Cu (1.12 min^{-1}). This demonstrates that Ni is the main catalytic active element in the CuCoNi system. Importantly, any combination of two components improves the TOF values compared to their unary counterparts, further validating the multi-component strategy. However, when Cu and Co, which individually exhibit lower activities, were combined into a binary alloy, the TOF of binary CuCo NPs (10.32 min^{-1}) remains lower than that of the unary Ni NPs (13.07 min^{-1}). This deeply highlighted the superior performance of Ni in catalyzing AB methanolysis for hydrogen generation.

In addition to catalytic activity, cyclic stability is also a critical indicator of the performance of catalysts. Ni, CoNi, and CuCoNi NPs@CAC samples were tested for 5 consecutive cycles of AB methanolysis for hydrogen generation. Figs. 5a-5c display the corresponding cyclic dehydrogenation curves, with specific TOF values and the percentage of residual activity after 5 cycles summarized in Fig. 5d and Table S4. After

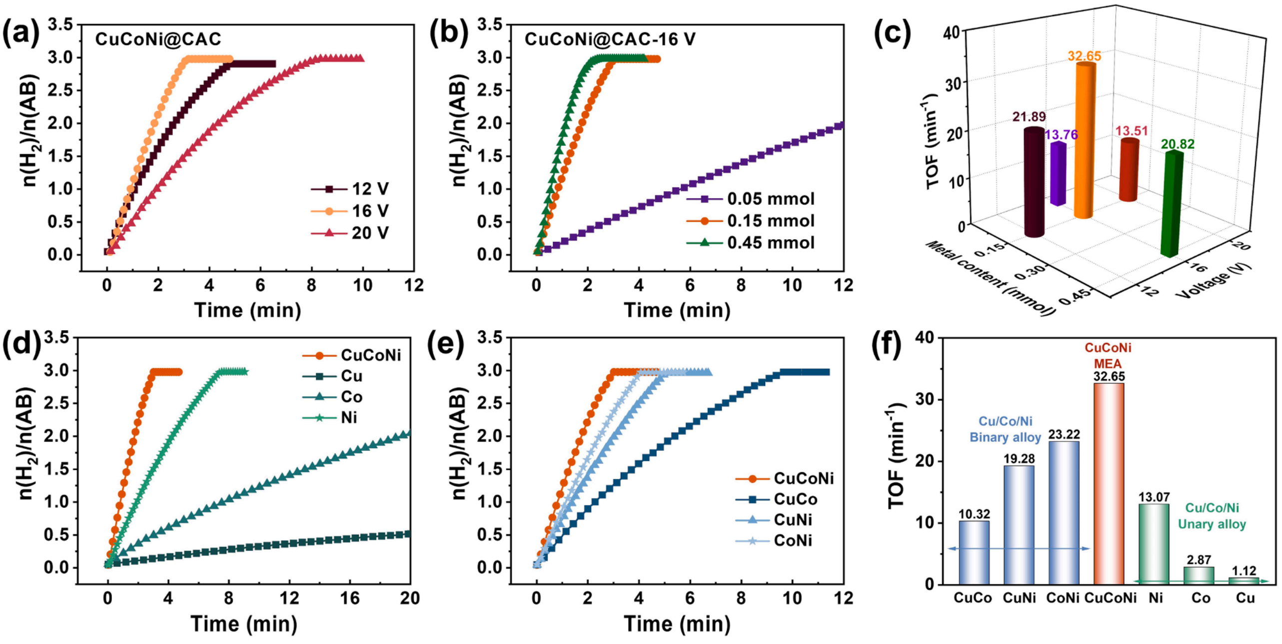

Fig. 4. a-c) Time-course plots of hydrogen generation for AB methanolysis and corresponding TOF values of the CuCoNi MEA NPs@CAC catalysts prepared with different discharge voltages and varying metal loadings. d-f) Time-course plots of hydrogen generation for AB methanolysis and the corresponding TOF values of the unary Cu/Co/Ni alloys, binary CuCo/CuNi/CoNi alloys, and the CuCoNi MEA catalysts prepared with the same discharge voltage and metal loadings.

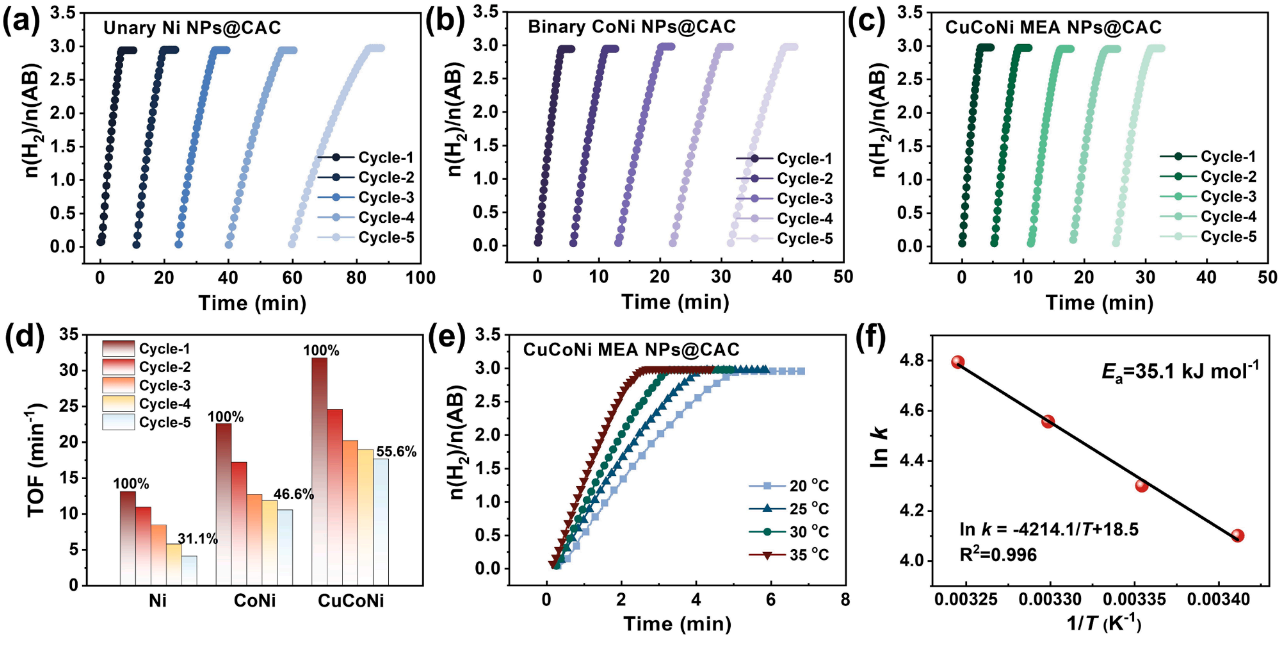

Fig. 5. a-c) Time-course plots of hydrogen generation for 5 cycles of AB methanolysis catalyzed by $Ni_{(0.15)}$, $CoNi_{(0.15)}$, and $CuCoNi_{(0.15)}$ NPs@CAC. d) TOF values and residual activity percentages of Ni, CoNi, and CuCoNi NPs@CAC after 5 cycles of AB methanolysis. e) Time-course plots of hydrogen generation for AB methanolysis catalyzed by $CuCoNi_{(0.15)}$ MEA NPs@CAC at different temperatures. f) Arrhenius plot of ln k vs. $1/T$ for $CuCoNi_{(0.15)}$ MEA NPs@CAC.

5 consecutive hydrogen release cycles, the TOF of Ni NPs@CAC retained only 31.1 % of its initial value. When components increased to CoNi binary, the residual activity percentage improved to 46.6 %, while CuCoNi exhibited the highest stability, retaining 55.6 % of its initial activity. The mixing entropy (ΔS_{mix}) of the alloys can be calculated using the following formula:

$$\Delta S_{mix} = -R\sum_{i=1}^{n} X_i \ln X_i \tag{4}$$

where R is the gas constant (8.314 J mol^{-1} K^{-1}) and X_{i} represents the mole fraction of each component in the system. The calculated values of ΔS_{mix} for Ni, CoNi, and CuCoNi are 0, 0.693 R, and 1.099 R. These results demonstrate that increasing the number of components improves the ΔS_{mix} of the alloy, thereby boosting catalytic stability through the "high-entropy effect".

Fig. 5e shows the hydrogen generation curves of CuCoNi MEA NPs@CAC at different reaction temperatures (T). The activation energy (E_{a}) was calculated by the Arrhenius equation:

$$\ln k = -\frac{E_a}{RT} + \ln A \tag{5}$$

where k is the rate constant (min^{-1}) of the catalytic reaction, R is 8.314 J mol^{-1} K^{-1}, T is the reaction temperature (K), E_a is the activation energy (J mol^{-1}), and A is the pre-exponential factor (s^{-1}). The E_a of CuCoNi MEA NPs@CAC was calculated to be 35.1 kJ mol^{-1}, which is relatively low compared with some previously reported non-noble metal catalysts [18,49–51]. A catalytic comparison of some other Cu/Co/Ni-based catalysts for AB methanolysis is presented in Table S5.

The catalytic performance comparison between CuCoNi MEA NPs@CAC synthesized by the CTS method and those prepared via the traditional reduction method is presented in Fig. S7. The hydrogen generation efficiency of the reduction-prepared CuCoNi MEA NPs@CAC is significantly slower than that of the CTS-prepared sample. Fig. S8 shows the STEM image and EDS mappings of the reduction-prepared sample, which displayed larger particle sizes and element aggregation. In contrast, the CTS method effectively achieved uniform mixing and melting of various elements, resulting in ultrafine sizes and homogeneous NPs distribution, thus exhibiting superior catalytic activity.

3.4. *Methanolysis catalytic mechanism*

Previous studies have proven that the rate-determining step (RDS) of AB hydrolysis catalysis is the scission of O-H in water [52]. Therefore, a kinetic isotopic effect (KIE) experiment was conducted to investigate whether the scission of the O-H bond in methanol is also the RDS of AB methanolysis [53]. As shown in Fig. 6a, CH_3OD was used in the AB methanolysis reaction. Under identical experimental conditions, both efficiency and amount of hydrogen generation from CH_3OD were considerably lower than that from CH_3OH, with a calculated KIE constant of 2.77. The large KIE constant suggests that bond cleavage is the RDS. Since the O-D bond is the only difference between CH_3OD and CH_3OH, it can be concluded that the O-H bond cleavage is the RDS in AB methanolysis.

To further understand the enhanced catalytic activity of CuCoNi MEA NPs@CAC compared to Ni NPs/CAC, the energy barrier associated with the RDS in the AB methanolysis was investigated through theoretical calculations (Fig. 6b). The energy required to break the O-H bond in CH_3OH is 0.412 eV for CuCoNi MEA NPs, which is lower than that of the Ni NPs (0.847 eV). This demonstrates that the CuCoNi MEA NPs catalyst exhibits superior catalytic kinetics in AB methanolysis compared to the unary Ni NPs, consistent with its higher TOF value.

A general schematic diagram of the AB methanolysis catalytic reaction is presented in Fig. 6c. Electron transfer occurs between AB and methanol that is promoted by the catalyst, leading to dehydrogenation and the formation of H_2. To further study the reaction mechanism catalyzed by CuCoNi MEA NPs, the average atomic charges of the Cu, Co, and Ni atoms in the FCC Ni, CuNi, CoNi, and CuCoNi alloys were calculated (Fig. S9). The unary Ni exhibits electrically neutral, but when Cu and Co are added, Ni becomes negatively charged. As the system reaches ternary components, the charge difference between Co (positive) and Ni (negative) reaches its maximum. Considering that Ni is the main active component, and the increase of negative charges of Ni is also similar to the growth of TOF, it is inferred that this value may be positively correlated with the catalytic activity. According to the DFT simulation results (Fig. 1), CuCoNi MEA provides a pathway for electron transfer between AB and methanol during the catalytic process.

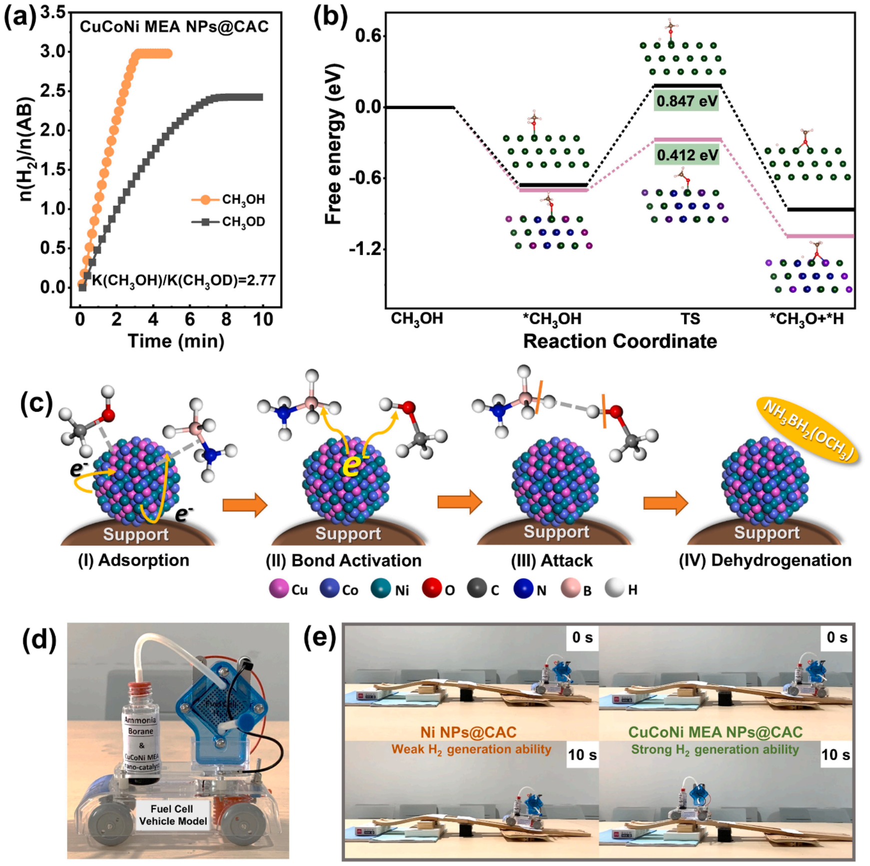

Fig. 6. a) Isotopic experiments of AB methanolysis catalyzed by $CuCoNi_{(0.15)}$ MEA NPs@CAC, using CH_3OH and CH_3OD as reactants. b) Energy barrier patterns of the RDS for the $Ni_{(0.15)}$ NPs and the $CuCoNi_{(0.15)}$ MEA NPs catalysts, inserting the structure models of catalyst and CH_3OH during the reaction process. c) Proposed AB methanolysis mechanism catalyzed by the $CuCoNi_{(0.15)}$ MEA NPs catalyst. d) Model of a fuel cell vehicle equipped with AB and the $CuCoNi_{(0.15)}$ MEA NPs@CAC catalyst. e) Performance comparison of the $Ni_{(0.15)}$ and the $CuCoNi_{(0.15)}$ NPs@CAC catalysts in AB methanolysis for hydrogen production driving the fuel cell vehicle.

Therefore, based on the AB hydrolysis mechanism and the above experimental results, the proposed AB methanolysis mechanism catalyzed by CuCoNi MEA NPs@CAC catalyst is outlined as follows:

(1) The CuCoNi MEA NPs@CAC adsorb AB and CH_3OH;
(2) The O-H bond in CH_3OH is activated by electrons provided by the negative Ni atoms and undergoes cleavage, resulting in the formation of *H and OCH_3^-;
(3) The OCH_3 species attacks the B atom of AB, leading to the generation of another *H and NH_3BH_2-OCH_3;
(4) Two *H combine to form H_2, which is subsequently released from the surface of the CuCoNi MEA NPs@CAC.

Fig. 6d presents a model of the fuel cell vehicle, powered by hydrogen produced from AB methanolysis. Using Ni NPs@CAC and CuCoNi MEA NPs@CAC as catalysts for the reaction, the vehicle exhibits varying power output performance. As shown in Fig. 6e, the superior hydrogen generation capability of CuCoNi MEA NPs@CAC in AB methanolysis enables the vehicle to accelerate up a slope within 10 seconds, whereas Ni NPs@CAC fails to achieve this. A video of the process is available in the supporting information. This result underscores the significance of developing high-performance catalysts for the practical application of hydrogen production via AB methanolysis.

Supplementary material related to this article can be found online at doi:10.1016/j.apcatb.2025.125140.

4. Conclusions

In summary, we determined that CuCoNi MEA is the optimized component for catalytic AB methanolysis through DFT simulation. An electronic structure of the catalyst that accelerates electron transfer between AB and methanol was achieved by regulating the *d*-band center. The CuCoNi MEA NPs@CAC catalyst with low-cost and high-activity was successfully synthesized using the CTS method. A series of experiments indicated that the discharge voltage and metal loading significantly influence the micromorphology of alloy particles, which impacts the catalytic activity. We determined the optimal synthesis parameters and prepared uniformly distributed CuCoNi MEA NPs with an average size of 15.8 nm, which exhibit an excellent TOF value of 32.65 min^{-1} in catalyzing AB methanolysis. Additionally, the experiments demonstrated that Ni displays the best catalytic performance for AB methanolysis within the Cu/Co/Ni series, whether in the unary, binary, or ternary alloy. Notably, both the catalytic activity and cycle stability were simultaneously enhanced through the multi-component strategy. This study innovatively introduces the CuCoNi MEA NPs in AB methanolysis, providing a novel approach for the development of high-performance catalysts and opening up significant opportunities for the application of medium-entropy alloys in the field of hydrogen energy.

CRediT authorship contribution statement

Fei Chu: Methodology, Investigation, Validation, Writing-original draft. **Jiahuan He:** Methodology, Investigation, Writing-review & editing. **Jinze Wang:** Investigation, Software, Writing-review & editing. **Nuo Lei:** Investigation, Methodology, Validation. **Sicheng Yuan**: Investigation, Methodology. **Shuoqing Zhang:** Investigation, Writing-review & editing. **Lixin Chen:** Supervision, Writing-review & editing. **Xuezhang Xiao:** Conceptualization, Investigation, Methodology, Supervision, Writing-review & editing, Funding acquisition.

Declaration of Competing Interest

The authors declare that they have no known competing financial interests or personal relationships that could have appeared to influence the work reported in this paper.

Acknowledgments

We are grateful for the financial support from the National Natural Science Foundation of China (52171223), and the Guangxi Science and Technology Major Project (AA24206007). We would like to thank Zhemin Wu and Qingyun Lin from the Center of Electron Microscopy of Zhejiang University for their technical assistance on TEM characterization.

Appendix A. Supporting information

Supplementary data associated with this article can be found in the online version at doi:10.1016/j.apcatb.2025.125140.

Data availability

Data will be made available on request.

References

[1] T. He, P. Pachfule, H. Wu, Q. Xu, P. Chen, Hydrogen carriers, Nat. Rev. Mater. 1 (2016).
[2] J. Graetz, New approaches to hydrogen storage, Chem. Soc. Rev. 38 (2009) 73–82.
[3] K. Jiao, J. Xuan, Q. Du, Z.M. Bao, B.A. Xie, B.W. Wang, Y. Zhao, L.H. Fan, H. Z. Wang, Z.J. Hou, S. Huo, N.P. Brandon, Y. Yin, M.D. Guiver, Designing the next generation of proton-exchange membrane fuel cells, Nature 595 (2021) 361–369.
[4] Y. Zhu, L. Ouyang, H. Zhong, J. Liu, H. Wang, H. Shao, Z. Huang, M. Zhu, Closing the loop for hydrogen storage: facile regeneration of $NaBH_4$ from its hydrolytic product, Angew. Chem. 132 (2020) 8701–8707.
[5] A. Kumar, P. Daw, D. Milstein, Homogeneous catalysis for sustainable energy: hydrogen and methanol economies, fuels from biomass, and related topics, Chem. Rev. 122 (2021) 385–441.
[6] B. Peng, J. Chen, Ammonia borane as an efficient and lightweight hydrogen storage medium, Energy Environ. Sci. 1 (2008) 479–483.
[7] S. Özkar, Transition metal nanoparticle catalysts in releasing hydrogen from the methanolysis of ammonia borane, Int. J. Hydrog. Energy 45 (2020) 7881–7891.
[8] H.-L. Jiang, Q. Xu, Catalytic hydrolysis of ammonia borane for chemical hydrogen storage, Catal. Today 170 (2011) 56–63.
[9] Q. Yao, Z.-H. Lu, K. Yang, X. Chen, M. Zhu, Ruthenium nanoparticles confined in SBA-15 as highly efficient catalyst for hydrolytic dehydrogenation of ammonia borane and hydrazine borane, Sci. Rep. 5 (2015) 15186.
[10] C.Y. Alpaydın, S.K. Gülbay, C.O. Colpan, A review on the catalysts used for hydrogen production from ammonia borane, Int. J. Hydrog. Energy 45 (2020) 3414–3434.
[11] W.-W. Zhan, Q.-L. Zhu, Q. Xu, Dehydrogenation of ammonia borane by metal nanoparticle catalysts, Acs Catal. 6 (2016) 6892–6905.
[12] D. Ozhava, S. Ozkar, Rhodium(0) nanoparticles supported on nanosilica: Highly active and long lived catalyst in hydrogen generation from the methanolysis of ammonia borane, Appl. Catal. B-Environ. 181 (2016) 716–726.
[13] D. Sun, V. Mazumder, O. Metin, S. Sun, Methanolysis of ammonia borane by COPD nanoparticles, Acs Catal. 2 (2012) 1290–1295.
[14] S. Guan, Y. Liu, H. Zhang, R. Shen, H. Wen, N. Kang, J. Zhou, B. Liu, Y. Fan, J. Jiang, Recent advances and perspectives on supported catalysts for heterogeneous hydrogen production from ammonia borane, Adv. Sci. (2023) 2300726.
[15] X. Li, Q. Yao, Z. Li, H. Li, Q.-L. Zhu, Z.-H. Lu, Porphyrin framework-derived N-doped porous carbon-confined Ru for NH_3BH_3 methanolysis: the more pyridinic-N, the better, J. Mater. Chem. A 10 (2022) 326–336.
[16] N. Kang, R. Shen, B. Li, F. Fu, B. Espuche, S. Moya, L. Salmon, J.-L. Pozzo, D. Astruc, Dramatic acceleration by visible light and mechanism of AuPd@ZIF-8-catalyzed ammonia borane methanolysis for efficient hydrogen production, J. Mater. Chem. A 11 (2023) 5245–5256.
[17] Y. Wang, J.L. Li, W.X. Shi, Z.M. Zhang, S. Guo, R. Si, M. Liu, H.C. Zhou, S. Yao, C. H. An, T.B. Lu, Unveiling single atom nucleation for isolating ultrafine fcc Ru nanoclusters with outstanding dehydrogenation activity, Adv. Energy Mater. 10 (2020).
[18] J. Liao, Y. Shao, Y. Feng, J. Zhang, C. Song, W. Zeng, J. Tang, H. Dong, Q. Liu, H. Li, Interfacial charge transfer induced dual-active-sites of heterostructured $Cu_{0.8}Ni_{0.2}WO_4$ nanoparticles in ammonia borane methanolysis for fast hydrogen production, Appl. Catal. B: Environ. 320 (2023).
[19] H.-J. Qiu, G. Fang, Y. Wen, P. Liu, G. Xie, X. Liu, S. Sun, Nanoporous high-entropy alloys for highly stable and efficient catalysts, J. Mater. Chem. A 7 (2019) 6499–6506.
[20] S.D. Lacey, Q. Dong, Z. Huang, J. Luo, H. Xie, Z. Lin, D.J. Kirsch, V. Vattipalli, C. Povinelli, W. Fan, Stable multimetallic nanoparticles for oxygen electrocatalysis, Nano Lett. 19 (2019) 5149–5158.
[21] M.W. Glasscott, A.D. Pendergast, S. Goines, A.R. Bishop, A.T. Hoang, C. Renault, J. E. Dick, Electrosynthesis of high-entropy metallic glass nanoparticles for designer, multi-functional electrocatalysis, Nat. Commun. 10 (2019) 2650.

[22] S. Ahmad, M. Egilmez, W. Abuzaid, F. Mustafa, A.M. Kannan, A.S. Alnaser, Efficient medium entropy alloy thin films as bifunctional electrodes for electrocatalytic water splitting, Int. J. Hydrog. Energy 52 (2024) 1428–1439.

[23] J.K. Pedersen, T.A. Batchelor, A. Bagger, J. Rossmeisl, High-entropy alloys as catalysts for the CO_2 and CO reduction reactions, Acs Catal. 10 (2020) 2169–2176.

[24] Z. Lv, X. Liu, B. Jia, H. Wang, Y. Wu, Z. Lu, Development of a novel high-entropy alloy with eminent efficiency of degrading azo dye solutions, Sci. Rep. 6 (2016) 34213.

[25] W. Al Zoubi, R.A.K. Putri, M.R. Abukhadra, Y.G. Ko, Recent experimental and theoretical advances in the design and science of high-entropy alloy nanoparticles, Nano Energy 110 (2023).

[26] Y. Xin, S. Li, Y. Qian, W. Zhu, H. Yuan, P. Jiang, R. Guo, L. Wang, High-entropy alloys as a platform for catalysis: progress, challenges, and opportunities, Acs Catal. 10 (2020) 11280–11306.

[27] Y. Yao, Q. Dong, A. Brozena, J. Luo, J. Miao, M. Chi, C. Wang, I.G. Kevrekidis, Z. J. Ren, J. Greeley, G. Wang, A. Anapolsky, L. Hu, High-entropy nanoparticles: Synthesis-structure-property relationships and data-driven discovery, Science 376 (2022) eabn3103.

[28] Y.-F. Liu, Y.-K. Huang, Y.-S. Guo, M.-Y. Yue, H.-X. Shao, Y.-J. Wang, NiCoFeCu medium-entropy alloy nanoparticles encapsulated in carbon nanotubes as catalysts for enhancing the hydrogen desorption of MgH_2, Rare Met. 43 (2024) 5868–5879.

[29] R. Yan, H. Yin, X. Zuo, W. Peng, X. Zhu, L. Shi, J. Hou, D. Wang, F. Ye, J. Li, Hollow PdCuCo medium-entropy alloy on reduced graphene oxide with proton-mediator boosted tandem catalysis for high-performance nitrate reduction, Appl. Catal. B: Environ. Energy 361 (2025) 124609.

[30] Q. He, J. Wang, H. Chen, Z. Ding, Z. Zhou, L. Xiong, J. Luan, J. Pelletier, J. Qiao, Q. Wang, A highly distorted ultraelastic chemically complex Elinvar alloy, Nature 602 (2022) 251–257.

[31] X. Zhang, Y. Yang, Y. Liu, Z. Jia, Q. Wang, L. Sun, L.C. Zhang, J.J. Kruzic, J. Lu, B. Shen, Defect engineering of a high-entropy metallic glass surface for high-performance overall water splitting at ampere-level current densities, Adv. Mater. (2023) 2303439.

[32] Y. Yao, Z. Huang, P. Xie, S.D. Lacey, R.J. Jacob, H. Xie, F. Chen, A. Nie, T. Pu, M. Rehwoldt, Carbothermal shock synthesis of high-entropy-alloy nanoparticles, Science 359 (2018) 1489–1494.

[33] S.B. Kalidindi, A.A. Vernekar, B.R. Jagirdar, Co-Co_2B, Ni-Ni_3B and Co-Ni-B nanocomposites catalyzed ammonia-borane methanolysis for hydrogen generation, Phys. Chem. Chem. Phys. 11 (2009) 770–775.

[34] X. Su, S. Li, PVP-stabilized Co–Ni nanoparticles as magnetically recyclable catalysts for hydrogen production from methanolysis of ammonia borane, Int. J. Hydrog. Energy 46 (2021) 14384–14394.

[35] Y. Feng, Y. Li, Q. Liao, W. Zhang, Z. Huang, X. Chen, Y. Shao, H. Dong, Q. Liu, H. Li, Modulation the electronic structure of hollow structured CuO-$NiCo_2O_4$ nanosphere for enhanced catalytic activity towards methanolysis of ammonia borane, Fuel 332 (2023).

[36] H. Li, Y. Han, H. Zhao, W. Qi, D. Zhang, Y. Yu, W. Cai, S. Li, J. Lai, B. Huang, L. Wang, Fast site-to-site electron transfer of high-entropy alloy nanocatalyst driving redox electrocatalysis, Nat. Commun. 11 (2020) 5437.

[37] Y. Chen, Q. Liu, J. Wang, Carbon dioxide activated carbon nanofibers with hierarchical micro-/mesoporosity towards electrocatalytic oxygen reduction, J. Mater. Chem. A 4 (2016) 5553–5560.

[38] G. Kresse, J. Furthmuller, Efficiency of ab-initio total energy calculations for metals and semiconductors using a plane-wave basis set, Comp. Mater. Sci. 6 (1996) 15–50.

[39] G. Kresse, D.J.Prb Joubert, From ultrasoft pseudopotentials to the projector augmented-wave method, Phys. Rev. B 59 (1999) 1758.

[40] N. Kharche, J.T. Muckerman, M.S. Hybertsen, First-principles approach to calculating energy level alignment at aqueous semiconductor interfaces, Phys. Rev. Lett. 113 (2014) 176802.

[41] F. Tong, X. Liang, Z. Wang, Y. Liu, P. Wang, H. Cheng, Y. Dai, Z. Zheng, B. Huang, Probing the mechanism of plasmon-enhanced ammonia borane methanolysis on a CuAg alloy at a single-particle level, ACS Catal. 11 (2021) 10814–10823.

[42] C. Wang, J. Tuninetti, Z. Wang, C. Zhang, R. Ciganda, L. Salmon, S. Moya, J. Ruiz, D. Astruc, Hydrolysis of ammonia-borane over Ni/ZIF-8 nanocatalyst: high efficiency, mechanism, and controlled hydrogen release, J. Am. Chem. Soc. 139 (2017) 11610–11615.

[43] T.D. Spivey, A. Holewinski, Selective interactions between free-atom-like d-states in single-atom alloy catalysts and near-frontier molecular orbitals, J. Am. Chem. Soc. 143 (2021) 11897–11902.

[44] Z.X. Li, C.C. Yu, Y.K. Kang, X. Zhang, Y.Y. Wen, Z.K. Wang, C. Ma, C. Wang, K. W. Wang, X.L. Qu, M. He, Y.W. Zhang, W.Y. Song, Ultra-small hollow ternary alloy nanoparticles for efficient hydrogen evolution reaction, Natl. Sci. Rev. 8 (2021).

[45] B.N. Mondal, A. Basumallic, P.P. Chattopadhyay, Magnetic behavior of nanocrystalline Cu-Ni-Co alloys prepared by mechanical alloying and isothermal annealing, J. Alloy Compd. 457 (2008) 10–14.

[46] Z. Dong, F.Y. Li, Q. He, X.Z. Xiao, M. Chen, C.T. Wang, X.L. Fan, L.X. Chen, PdCoNi nanoparticles supported on nitrogen-doped porous carbon nanosheets for room temperature dehydrogenation of formic acid, Int. J. Hydrog. Energy 44 (2019) 11675–11683.

[47] H. Yen, F. Kleitz, High-performance solid catalysts for H_2 generation from ammonia borane: Progress through synergetic Cu–Ni interactions, J. Mater. Chem. A 1 (2013) 14790–14796.

[48] G. Pacchioni, H.-J. Freund, Controlling the charge state of supported nanoparticles in catalysis: lessons from model systems, Chem. Soc. Rev. 47 (2018) 8474–8502.

[49] M. Yurderi, A. Bulut, I.E. Ertas, M. Zahmakiran, M. Kaya, Supported copper-copper oxide nanoparticles as active, stable and low-cost catalyst in the methanolysis of ammonia-borane for chemical hydrogen storage, Appl. Catal. B-Environ. 165 (2015) 169–175.

[50] D. Ozhava, N.Z. Kilicaslan, S. Ozkar, PVP-stabilized nickel(0) nanoparticles as catalyst in hydrogen generation from the methanolysis of hydrazine borane or ammonia borane, Appl. Catal. B-Environ. 162 (2015) 573–582.

[51] J. Zhang, Y. Duan, Y. Zhu, Y. Wang, H. Yao, G. Mi, Evenly dispersed microspherical amorphous alloy Co_xB_{1-x}: Robust and magnetically recyclable catalyst for alcoholyzing ammonia borane to release H_2, Mater. Chem. Phys. 201 (2017) 297–301.

[52] F. Yao, S. Guan, L. Bian, Y. Fan, X. Liu, H. Zhang, B. Li, B. Liu, Ensemble-exciting effect in Pd/alk-Ti3C2 on the activity for efficient hydrogen production, ACS Sustain. Chem. Eng. 9 (2021) 12332–12340.

[53] X. Li, Q. Yao, R. Shi, M. Huang, Z.H. Lu, A step-growth strategy to grow vertical porous aromatic framework nanosheets on graphene oxide: Hybrid material-confined Co for ammonia borane methanolysis, Carbon Energy 5 (2023) e357.